PHYSICS OF PLASMAS VOLUME 5, NUMBER 4 APRIL 1998

Spectroscopic determination of the magnetic-field distribution in an imploding plasma

G. Davara, L. Gregorian, E. Kroupp, and Y. Maron
Faculty of Physics, Weizmann Institute of Science, Rehovot, 76100, Israel

(Received 4 November 1997; accepted 13 November 1997)

The time-dependent radial distribution of the magnetic field in a high density z-pinch plasma has been determined by observation of the contribution of the Zeeman effect to the spectral profiles of ionic emission lines. The dominance of the line profiles by the Stark broadening required high-accuracy profile measurements and the use of polarization spectroscopy. The plasma implodes in $\simeq 600$ ns, and the field distribution was measured up to 90 ns before stagnation on axis. During the implosion the plasma was found to conduct the entire circuit current. By comparing the data to the solution of the magnetic diffusion equation the electrical conductivity of the plasma was determined, found to be in agreement with the Spitzer value. These measurements, together with our previously measured ion velocity distributions, allowed for the determination of the time-dependent relative contributions of the magnetic and thermal pressure to the ion radial acceleration across the plasma shell. © *1998 American Institute of Physics.* [S1070-664X(98)01704-2]

I. INTRODUCTION

Hot and dense plasmas produced in pulsed-power-driven z-pinch devices have been extensively investigated over the past several decades due to their relevance to controlled nuclear fusion research,[1–5] x-ray laser research,[6] x-ray lithography,[7,8] and radiation sources.[2] A z-pinch load, typically consisting of a cylindrical gas column or of a wire array, is imploded by the magnetic pressure which is produced by the axial current. At stagnation, the kinetic energy of the imploding plasma is converted to heating and radiation.

Knowledge of the magnetic-field distribution in a z-pinch plasma is of high importance since the plasma-field interaction plays a key role in determining the characteristics of the pinch core and the efficiency of the energy coupling to the plasma. Various theoretical models and simulation schemes of z-pinch plasmas[1,9,10] strongly rely on the magnetic-field distribution for predictions of the hydrodynamic and atomic processes in the plasma. Furthermore, determination of the magnetic-field distribution can serve for studying the properties of the imploding plasma. Recently, the Faraday rotation technique has been used to measure the magnetic field within a radius of $\leqslant 0.5$ mm in a metallic wire explosion z-pinch experiment.[11]

In this report, we describe the time-dependent measurements of the magnetic-field distribution throughout the implosion phase of a moderate density, gas-puff z-pinch plasma, using observations of the Zeeman effect contribution to the spectral profiles of line emission from various charge-state oxygen ions. The field distribution allowed for determining the plasma electrical conductivity, for the first time in such imploding plasmas. We used the experimentally obtained time-dependent boundary conditions to solve a one-dimensional (1D) magnetic diffusion equation, which gave a conductivity consistent with the Spitzer value, known from the independently determined electron temperature. The current density obtained from the magnetic-field distribution was compared to the total discharge current, independently measured by a Rogowski loop, where it was found that up to 60 ns before the pinch most of the current flows within the imploding plasma column. Furthermore, the obtained $\mathbf{J}\times\mathbf{B}$ forces across the plasma shell are compared to the total radial acceleration of various charge-state ions previously observed from spectral line Doppler shifts.[12] This allows for determining the contributions of both the magnetic field and thermal pressure gradients to the ion acceleration.

II. EXPERIMENTAL ARRANGEMENT

A schematic of the z-pinch experiment is given in Fig. 1. The gas-puff system, consisting of a fast electromagnetic valve and an annular nozzle (cathode), is used to produce a hollow cylinder of gas ($R\simeq 2$ cm, $\delta R\simeq 0.5$ cm) in the 1.35 cm wide anode-cathode gap, where the anode is a hollow tube, 4 cm in diameter. A high-voltage discharge circuit, powered by a 25 kV, 16 μF capacitor bank, produces a peak current of 320 kA with a rise time of 1.6 μs. The operating gas throughout the present experiments was CO_2, as in the previous study.[12] The pinch occurs at $t\simeq 620$ ns (with an irreproducibility of $\simeq 3\%$) relative to the beginning of the current pulse, with the total axial current at this time being $\simeq 220$ kA, as shown by the Rogowski coil measurement given in Fig. 1.

The diagnostic setup, also shown in Fig. 1, includes two ultraviolet (UV) spectroscopic systems, allowing for simultaneous observations of a few line emissions or different emission polarizations along the z axis (end-on), along the radius (side-on), and along various chords of the cylindrical plasma. The two systems include a 1.26 and 1.1 m spectrometers, both equipped with 2400 grooves/mm gratings. The output slit of the spectrometer of one system is coupled to a fast UV-visible streak camera, operated at a sweep speed of 1 μs/25 mm. A cooled 1024×1024-pixel CCD (charge-coupled device) is lens-coupled to the streak camera and

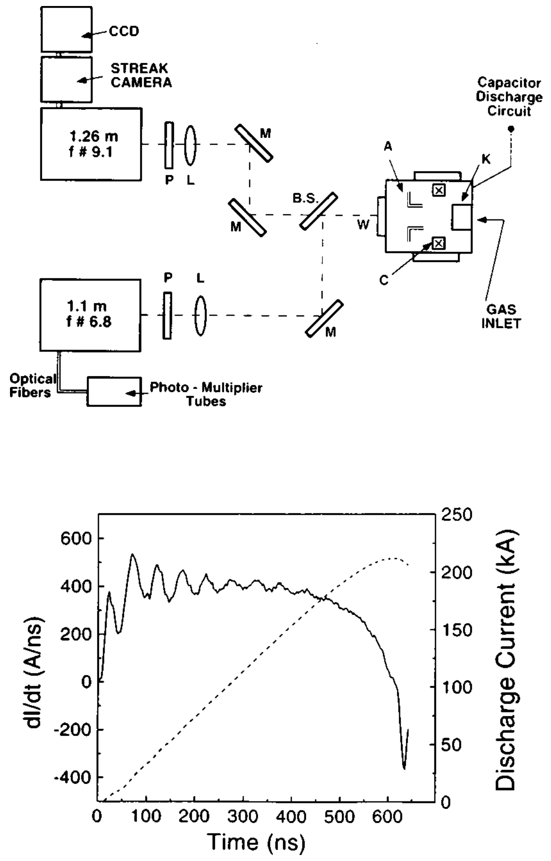

FIG. 1. A schematic of the z-pinch experiment and the diagnostic systems. W, L, M, and $B.S.$ are a window, a lens, a mirror, and a beam splitter, respectively. The polarization of the collected emission is selected by the use of a rotatable $\lambda/2$ plate P. Also shown are the traces of dI/dt (solid line) and the total current I (dashed line) measured by a Rogowski coil C placed around the plasma.

records its two-dimensional output image. The output of the other spectrometer is coupled via optical fibers to 12 UV-visible photomultiplier tubes, the signal of which is recorded by digital oscilloscopes.

In the measurements, the temporal and spectral resolutions for the different emission lines observed were determined by varying the averaging extent of the readout system. Usually, the temporal resolution was 10 ns and the spectral resolution $\simeq 0.1$ Å, much smaller than the linewidths observed in this study. The spatial resolution was determined by the dimensions of the input slit of the spectrometer.

A beam splitter was used in experiments in which the two systems were used for simultaneous observations. The sensitivity of each system to the different polarizations was measured using calibrated external light sources.

III. EXPERIMENTAL TECHNIQUE

Line emission in the presence of magnetic-field undergoes wavelength shifts $\Delta\lambda$ (in Å) of the π (linear polarization) and σ (circular polarization) components relative to the line center, which in the weak field limit are given by

$$\Delta\lambda_{\pi} = 10^{-8}\,\frac{\mu_0 B}{\hbar c}\,\{g_u - g_l\}\,m\lambda_0^2,$$

$$\Delta\lambda_{\sigma} = 10^{-8}\,\frac{\mu_0 B}{\hbar c}\,\{g_u m - g_l(m \pm 1)\}\,\lambda_0^2, \qquad (1)$$

where B is the magnetic-field strength in Gauss, μ_0 is the Bohr magneton (9.27×10^{-21} erg/Gauss), λ_0 is the wavelength of the nonperturbed line in Å, m is the projection of the total angular momentum, and g_u and g_l are the Landè factors of the upper and lower levels, respectively.

The main difficulty in observing Zeeman splitting of line emission from imploding plasmas is caused by the line broadening due to other mechanisms, namely the Stark, Doppler, and absorption effects. It was verified that for all emission lines used in this study the Stark broadening (here calculated using the methods described in Ref. 13) strongly dominated the line profiles during the implosion phase. This required the use of polarization optics in order to observe the relative contributions of the π and σ components to the spectral widths of the observed lines, and thus to discriminate the Zeeman splitting against other broadening mechanisms.

The measurements were carried out by observing the plasma along the z axis at various radial locations. Such axial observations were used in our previous study where, as described in Ref. 12, it was shown that an ionization front propagates in the plasma, so that at any instant the higher charge-state ions reside at radii larger than those of the lower charge-state ions. It was also found that for a given radial position the dominant charge state in the plasma rises in time. This time-dependent radial distribution of the charge state provided a complete mapping in (r,t) of the line emission from the plasma, thus allowing for time-dependent measurements of Zeeman splitting of spectral lines at various radial locations across the plasma shell to be made.

In the axial measurements, the line emission is collected perpendicular to the magnetic-field lines, therefore both the π and σ components are observed. For the selection of the π or σ components, we used a half-wave plate (see Fig. 1) to rotate the polarization plane of the collected line emission, and utilized the higher reflectivity of the spectrometer gratings for light polarized parallel to the grooves (for the spectral range of interest, 2700–3900 Å, the reflectivity for the polarization parallel to the grooves is about seven times higher than that for the normal polarization).

The configuration of the observations is shown in Fig. 2. The vertical dimension of the spectrometer input slit is parallel to the azimuthal dimension of the plasma region observed. In the present study, the azimuthal and radial dimensions of this region are $\Delta h = 2$ mm and $\Delta r = 0.4$ mm, respectively. The magnetic field was observed for radii $r \geqslant 7$ mm. For these conditions the curvature of the magnetic field along the azimuthal dimension within the observed plasma region had insignificant effect on the polarization properties of the line emission in the observation direction.

The axial nonuniformity in the imploding plasma was studied in detail[14] in order to determine the degree of uncertainty caused by the spatial integration of the measurement along the plasma axial dimension. This study was carried out

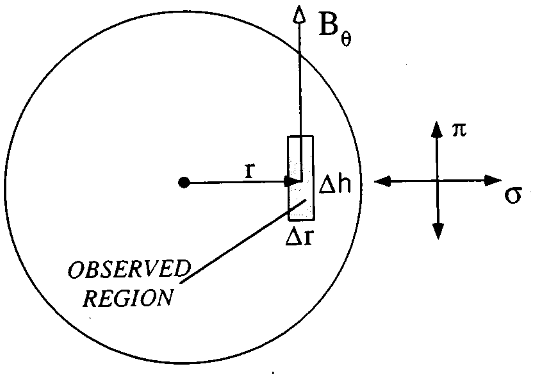

FIG. 2. A schematic of the plasma region observed in the z direction. Δh and Δr are determined by the size of the input slit of the spectrometer; typical values are 2 and 0.4 mm, respectively. The radial position r was $\geqslant 7$ mm throughout the measurements.

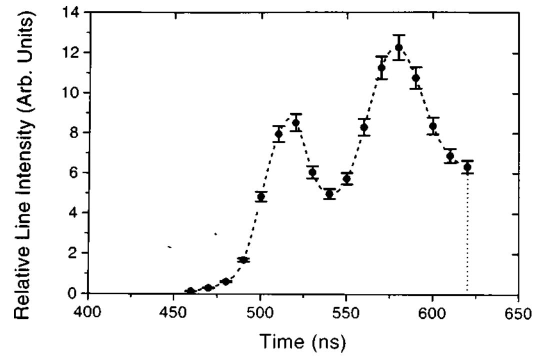

FIG. 4. Typical result of the time-dependent line intensity obtained in an axial observation at a given radial position. The first and the second peaks correspond to line emission from the plasma regions close to the anode and to the cathode, respectively. The pinch time ($\simeq 620$ ns) is marked by the vertical dashed line.

by observing the line emission from the imploding plasma along various chords at different axial positions. In brief, these measurements showed that for the radial positions relevant for this study ($r \geqslant 7$ mm), the plasma in the region near the anode implodes significantly earlier than the rest of the plasma column. Consistently, at a given instant of time, ions of a given charge state within 4 mm near the anode reside at smaller radii than those farther from the anode, as can be seen in the example given in Fig. 3, where the z-dependent radial positions of the various charge-state ''clouds'' are presented for $t \simeq 520$ ns.

These findings are consistent with the results of the axial observations carried out in our previous study,[12] the typical example of which is presented in Fig. 4. Given in this figure is the time-dependent line intensity of the **OIV** line (3063.47 Å), as obtained from an axial observation at $r = 10$ mm. The first and the second peaks of the recorded intensity correspond to the appearance of line emission from the plasma near the anode and near the cathode, respectively. The time delay between the peaks ($\simeq 70$ ns) is much larger than the integration time of the present measurements ($\simeq 10$ ns). Therefore, due to this relatively long time delay between the formation of each charge state near the anode and the cathode, the axial measurements described below give the radial distribution of the magnetic field only within the region of $\simeq 4$ mm near the anode. The small z-dependence in this limited region near the anode allows for reliably obtaining averaged values of line widths and intensities.

IV. MEASUREMENTS AND RESULTS

First, the time-dependent radius of the outer boundary of the plasma was determined based on the radial distribution of charge state (see previous section). At each instant the total light intensity, observed at a radius $\simeq 0.05$ cm larger than that of the highest charge-state radial position, was found to be orders of magnitude lower than in the plasma. The radius at which this sharp drop in the light intensity occurs is here referred to as ''the outer radius'' R_0 of the plasma. A plot of R_0 as a function of time is given in Fig. 5, showing that the radial motion of the plasma started at $t \simeq 320$ ns. Also given in Fig. 5 is the boundary magnetic field $B_0(t)$ (Tesla) defined by

$$B_0(t) = B(r = R_0(t), t) = 0.02\,\frac{I(t)}{R_0(t)}, \tag{2}$$

obtained assuming the entire circuit current $I(t)$ (kA) flows within a cylinder bound by R_0 (cm). It is seen in Fig. 5 that

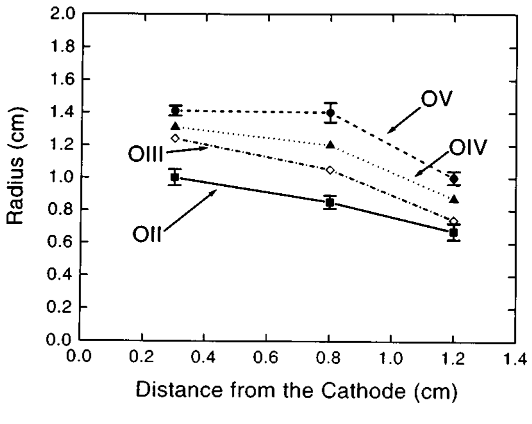

FIG. 3. An example of the results of the chord measurements. Shown are the radial positions of the various charge-state ions as a function of z at $t = 520$ ns.

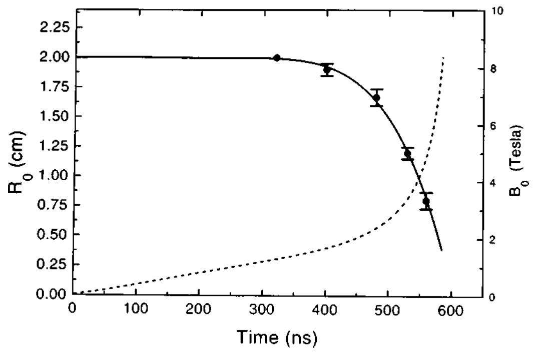

FIG. 5. The observed outer radius of the plasma $R_0(t)$. The solid line is a smooth curve through the data points. Also shown is the boundary field $B_0(t)$, obtained from Eq. (2) using the curves for $I(t)$ (given in Fig. 1) and $R_0(t)$.

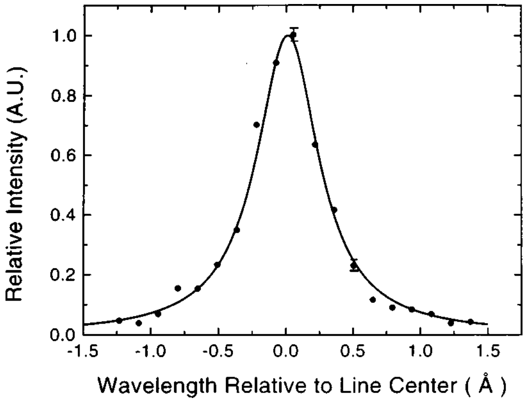

FIG. 6. Typical line-profile of the **OIV** $3s-3p$ (3063.5 Å) transition, measured at $r=1.65$ cm and $t=480$ ns. The solid line is a best-fit Lorentzian to the data (see text).

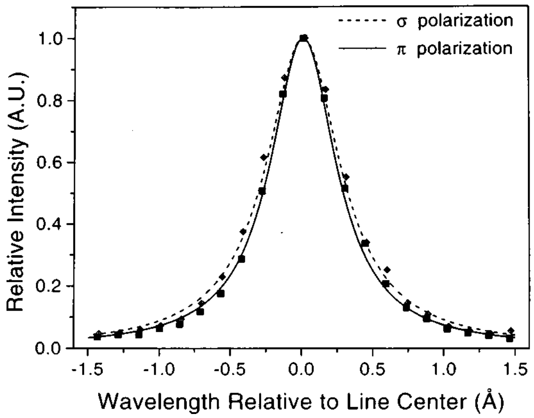

FIG. 7. Measured profiles for the σ and π polarizations of the **OIV** 3063.5 Å line for $t=480$ ns, each obtained by averaging 20 repeated discharges. The uncertainties are given by the size of the data points in the figure. The FWHM of the Lorentzian fits are 0.56 ± 0.01 Å (π) and 0.62 ± 0.01 Å (σ). The uncertainty in the FWHM is determined from the difference between the widths of profiles fitted to the upper or lower bounds of the data points. Here, B_θ obtained is 1.8 ± 0.3 Telsa.

the boundary magnetic field starts its significant rise at $t \simeq 400$ ns. Presented below are the results of measurements of the magnetic-field distribution for three times ($t=480$, 530, and 560 ns), selected from our time-dependent data to describe the rise of the magnetic field during the period of the radial motion of the plasma.

In the measurements, the π- and σ-polarized radiation from the same plasma volume was either collected simultaneously by the two spectroscopic systems (using a half-wave plate for one of them, as described in the previous section), or using one system, for which the two polarization components were measured in different discharges. Relative to the nonsimultaneous observations, the use of a beam splitter in the simultaneous observations resulted in lower line intensities and thus lower signal-to-noise ratios for each of the spectroscopic systems. This limited the use of the simultaneous observations to the intense lines, therefore, the nonsimultaneous observations were found to be preferable for most of the measurements described below. The results of the simultaneous measurements for the strong lines, however, were used to demonstrate the satisfactory agreement between the simultaneous and the nonsimultaneous observations (see below).

Figure 6 gives an example of a measurement. Shown is a typical profile of the σ-polarized emission of **OIV** ($3s-3p$ transition at 3063.47 Å), obtained in a single discharge for $r=1.65$ cm and $t=480$ ns. Here, the spectral and temporal resolutions are 0.14 Å and 10 ns, respectively. The fitting curve used in Fig. 6, as for all the data presented below, is Lorentzian, consistent with the dominance of the Stark effect in the line broadening, as found for all lines used in the present study (the contribution of the ion temperature is too small to affect the line profile, as shown in Ref. 15). For the data given in Fig. 6, the uncertainty in each point, mainly resulting from the statistical fluctuations due to the limited number of photons, is between $\pm1\%$ to $\pm2.5\%$. This gives rise to an uncertainty of $\simeq4\%$ in the FWHM (full width at half maximum) of the fitted curve. The uncertainty in the FWHM is obtained from fitting curves to the upper and lower bounds of the error bars of each point.

In the nonsimultaneous measurements, shot-to-shot variations of $\simeq10\%$ in the linewidths for a given radius and time were observed, resulting from the irreproducibility of the electron density (that affects the Stark line broadening) in the different discharges. Therefore, in order to improve the accuracy in the spectral linewidths obtained, the observations were repeated for each radius and polarization. Averaging each data point of the spectral profile over N discharges reduces the uncertainty in the line FWHM by $(N-1)^{-1/2}$. Examples of average profiles of the **OIV** $3s-3p$ transition (3063.47 Å), obtained from 21 measurements for each polarization direction for $r=1.65$ cm and $t=480$ ns, are given in Fig. 7. Each curve is a best-fit Lorentzian to the averaged profile, giving an uncertainty of $\pm2\%$ in the line FWHM.

The fits shown in Fig. 7 give FWHM of 0.56 ± 0.01 and 0.62 ± 0.01 Å for the π and σ components, respectively. The fitted line profiles are then compared to a computer calculations of line profiles based on the Zeeman splitting of the Stark broadened lines. In this calculation, the magnetic-field strength and the FWHM of the Stark broadened Lorentzian profile are used as parameters. This comparison yields these two parameters self-consistently. For the example given in Fig. 7, the magnetic field obtained using this procedure is 1.8 ± 0.3 Tesla. The electron density obtained from the linewidth is discussed in detail separately[15] (for this example the electron density inferred is $5\pm1.5\times10^{17}$ cm^{-3}).

Part of the results of the magnetic-field measurements are presented in Table I. Given are the wavelengths of the observed lines and the measured values of the linewidths for the two polarizations used for the determination of the magnetic field for several times and radii. The data for each polarization represents an average of 20–38 discharges. Also given in Table I is the distance $\xi=R_0(t)-r$, which is the radial position relative to the outer plasma boundary at time t.

For certain radii and times the magnetic field was determined using a few different emission lines. For example, the

TABLE I. Magnetic-field strength at various times and radii, obtained from the measured spectral line profiles for the π and σ emission components. r and t are the radius and time of observation, and ξ is the distance from the outer radius of the plasma. λ_0 is the unperturbed wavelength of the line observed (the charge state is given in brackets). $\Delta\lambda_\sigma$ and $\Delta\lambda_\pi$ are the FWHM for the σ and π polarizations, respectively, and $\Delta\lambda_0$ is the unfolded zero-magnetic-field spectral width due to Stark broadening (see text).

r(cm)	t(ns)	λ_0(Å)	$\Delta\lambda_0$(Å)	$\Delta\lambda_\pi$(Å)	$\Delta\lambda_\sigma$(Å)	ξ(cm)	B_θ(T)
1.65	480±3	3063.47(OIV)	0.55±0.01	0.56±0.01	0.62±0.01	0.02	1.8±0.3
1.67	463±4	3047.13(OIII)	0.50±0.01	0.50±0.01	0.51±0.01	0.15	<0.7
1.2	507±3	3047.13(OIII)	0.43±0.01	0.43±0.01	0.48±0.01	0.27	0.9±0.2
1.2	530±2	3144.68 (OV)	1.00±0.03	1.02±0.02	1.11±0.02	0	3.4±0.3
1.05	530±2	3063.47(OIV)	0.57±0.01	0.58±0.01	0.63±0.01	0.15	1.6±0.2
0.85	530±3	3047.13(OIII)	0.48±0.01	0.48±0.01	0.52±0.01	0.35	1.0±0.2

magnetic-field intensity at $r=1.2$ cm and $t=530$ ns, obtained from measurements of the 3144.7 Å line of **OV**, gave a value of 3.4±0.3 Tesla, see Table I. The values obtained from measurements of the **OV** 2781.0 and 2787.0 Å lines for the same radius and time (not included in the table) were 3.2±0.3 and 3.6±0.4 Tesla, respectively, in a good agreement (to within the error bar) with that obtained using the 3144.7 Å line.

Several measurements of the **OV** 3144.7 Å and the 2781.0 Å lines at $r=1.2$ cm and $t=530$ ns have been carried out using both spectroscopic systems, simultaneously observing the π and σ components of the line profiles. The value of the magnetic field obtained from both lines was 3.5±0.3 Tesla, which agrees with that obtained in the non-simultaneous measurements, see Table I. However, as mentioned above the simultaneous measurements, resulting in less light collected by each spectroscopic system, were less preferable for the weaker lines.

In Fig. 8 we present the radial distribution of the magnetic field for the times 480 and 530 ns, based on the data points given in Table I. The value of the magnetic-field strength at $t=480$ ns and $r=1.4$ cm ($\xi=0.27$ cm) is 0.7 ±0.35 Tesla. It was obtained from interpolation of the data at $t=463$ ns and $t=507$ ns, where the magnetic field was measured at $\xi=0.15$ and $\xi=0.27$ cm, respectively (see Table I). Such an interpolation is justified, based on the monotonic behavior and the slow variation of the magnetic field across the plasma shell over this time interval. Also indicated are the outer plasma radius R_0 and the field B_0 [obtained from R_0 and the circuit current, see Eq. (2)] for each time. It is seen that for both times the values of the magnetic field measured near R_0 agree with B_0, indicating that most of the circuit current flows within the outer diameter of the plasma.

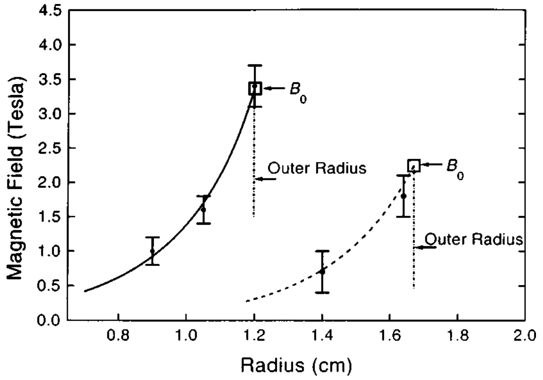

FIG. 8. The magnetic-field distribution in the plasma at $t=480$ and $t=530$ ns. The fitting curves are based on the solution of a 1D magnetic-field diffusion equation for each time using the plasma conductivity σ as indicated (see Sec. V). The boundary field B_0, represented by the squares, is obtained from Fig. 5.

For $t=560$ ns, closer to the stagnation, we measured the magnetic-field strength at $r=0.75$ cm using line emission of **OV** ions, where the outer radius R_0 at this time was 0.8 cm, determined from measurements of **OVI** line emission. The value obtained, 3.6±0.5 Tesla, shows that also at this time most of the circuit current flows within the outer diameter of the plasma [B_0 calculated using Eq. (2) is $\simeq 4.7$ Tesla]. The radial distribution of the magnetic field, however, could not be determined for this time because of large uncertainties in the spectral line profiles caused by the axial nonuniformity of the line emission.

V. DISCUSSION

The data presented above allow us to model the magnetic-field penetration into the z-pinch plasma in order to determine the plasma electrical conductivity. To this end, we solve the magnetic diffusion equation (in which the Hall-current term is neglected, which is justified for our plasma density)

$$\frac{\partial \mathbf{B}}{\partial t}=\nabla\times(\mathbf{v}\times\mathbf{B})-\frac{c^2}{4\pi}\nabla\times\left(\frac{1}{\sigma}\nabla\times\mathbf{B}\right), \tag{3}$$

where $\mathbf{v}$ is the particle velocity and σ is the plasma conductivity. Having established that most of the current in the circuit flows within the outer diameter ($2R_0$) of the plasma, our data provide the boundary condition $B_0(t)$ for this equation, based on the experimentally determined $I(t)$ and $R_0(t)$, see Eq. (2). Here, we solve the equation using a single averaged value for the plasma conductivity σ, and assuming a motionless plasma. The particle velocities relative to the moving outer boundary, measured in the plasma region in which a significant magnetic field is observed, were $\simeq 3\cdot 10^6$ cm/s (see Ref. 12). The neglect of these velocities is estimated to give rise to an uncertainty of factor $\leqslant 2$ in the value of the plasma conductivity inferred below. In addition, planar geometry is employed, since for the times and the radial region presently considered the neglect of the cylindrical terms is estimated to little affect the solution.

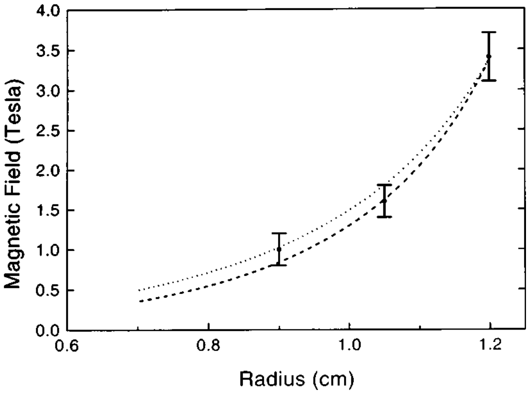

FIG. 9. Solutions of the magnetic diffusion equation using $\sigma = 2.0\times10^{14}\ \mathrm{s}^{-1}$ (dotted line) and $\sigma = 2.8\times10^{14}\ \mathrm{s}^{-1}$ (dashed line), both calculated for $t = 530$ ns, together with the experimental data points for this time.

Based on these assumptions, Eq. (3) can now be written in its simplified form

$$\frac{\partial B_\theta}{\partial t} = \frac{c^2}{4\pi\sigma}\,\frac{\partial^2 B_\theta}{\partial \xi^2},$$
$$B_\theta(\xi,0) = 0, \quad B_\theta(\xi = 0,t) = B_0(t), \tag{4}$$

where $\xi = R_0(t) - r$. We assume a finite thickness (slab) geometry, $0 < \xi < l$, where l is the thickness of the plasma shell. For an arbitrary boundary condition $B_0(t)$ and constant conductivity, the solution is[16]

$$B(\xi,t) = \frac{\sqrt{\sigma}}{c}\int_0^t \frac{B_0(\tau)}{(t-\tau)^{3/2}} \times \sum_{n=-\infty}^{+\infty}\left\{(\xi + 2nl)\exp\left[-\frac{\pi\sigma(\xi + 2nl)^2}{c^2(t-\tau)}\right]\right\} d\tau, \tag{5}$$

where t is the time of observation. Solving for various values of the shell thickness l, it was found that the solution is insensitive to $l \geqslant 0.5$ cm. For the solution described below we used $l = 0.7$ cm, since this was the measured thickness of the plasma shell for all the times at which a significant magnetic field was observed ($t > 400$ ms, see Fig. 5), i.e., the times that most contribute to the integral in Eq. (5).

Numerical solutions of Eq. (5), using the plasma conductivity σ as a parameter, were used to fit the measured magnetic-field distributions for various times during the implosion, in order to determine the experimental value of σ. For example, given in Fig. 9 is the field distribution for $t = 530$ ns, together with solutions using σ-values that fit the upper and lower bounds of the error bars of the data points. It is seen that for this example, as for all times during the implosion, the data accuracy allows for determining σ to within a factor of $\simeq 2$. In Fig. 8 we present examples of best-fit solutions for the magnetic-field distributions for $t = 480$ and $t = 530$ ns, giving $\sigma = 2.8 \pm 1.0\times10^{14}\ \mathrm{s}^{-1}$ ($3.1 \pm 1.1\times10^4\ \mathrm{Ohm}^{-1}\,\mathrm{m}^{-1}$) and $\sigma = 2.4 \pm 0.4\times10^{14}\ \mathrm{s}^{-1}$ ($2.7 \pm 0.4\times10^4\ \mathrm{Ohm}^{-1}\,\mathrm{m}^{-1}$), respectively. The resultant skin depth, defined as the e-fold decrease in the field intensity, is 0.24 ± 0.05 cm for $t = 480$ ns and 0.23 ± 0.02 cm for $t = 530$ ns.

We now compare these best-fit values for σ to the Spitzer value, known from an independent determination of the radial distributions of the electron temperature and the charge state in the plasma.[15] At $t = 530$ ns, for example, T_e obtained was between 5 ± 1 eV in the inner region of the plasma (determined from lines of **OII** that dominate the plasma at this region) and 13 ± 2 eV in the outer region of the plasma (dominated by **OV**). The Spitzer conductivity obtained from such data was found to vary by $\sim 50\%$ across the plasma shell for all times of interest, giving an averaged value of $\sigma \simeq (1.9 \pm 0.6)\times10^{14}\ \mathrm{s}^{-1}$ ($2.1 \pm 0.7\times10^4\ \mathrm{Ohm}^{-1}\,\mathrm{m}^{-1}$). This value is in good agreement with the values obtained from the fits to the experimental data, in which a single-value for the conductivity was assumed in the solution of Eq. (3), as said above. It is therefore concluded that during the early implosion the plasma conductivity is nearly Spitzer. This conclusion is expected on theoretical grounds in the absence of ion acoustic[17] and lower hybrid[18] instabilities, which probably results from the high plasma collisionality.

Using the experimental results given above, together with the results of our previous study,[12] it is now possible to determine the radial acceleration of ions across the plasma shell, and further to obtain the thermal pressure gradient as a function of time and radius. It is shown in Ref. 12 that our data allow for following the velocity rise of a fluid element as it ionizes into higher charge states, since the time it is encountered by the ionization front that moves radially inward ahead of the imploding shell. Then, using the present results, we calculate the **J×B** forces acting on this fluid element as it moves across the plasma shell. The time-dependent ion acceleration due to the thermal pressure gradient is then obtained by subtracting the contribution of the **J×B** forces from the total radial acceleration of the ions.

Consider a gas element denoted by a subscript α, residing at $r_0 = r(t_0)$, where t_0 is the time the gas element is encountered by the ionization front and is ionized into singly charged ions. The radial position $r(t)$ of the fluid element at time t is given by

$$r(t) = r(t_0) + \int_{t_0}^{t} v_\alpha(r(t'),t')\,dt'. \tag{6}$$

Here $v_\alpha(r(t'),t')$ is the measured radial velocity of ions of the fluid element α. The **J×B** force acting on an ion in the fluid element is described by

$$F_R(r,t) = \frac{1}{c n_\alpha(r,t)}\,J_z(r,t)\cdot B_\theta(r,t)$$
$$= \frac{Z_\alpha(t)}{c n_e(r,t)}\,J_z(r,t)\cdot B_\theta(r,t), \tag{7}$$

where n_α is the ion density, and $Z_\alpha(t)$ is the time dependent effective charge of the fluid element considered. The variation in time of Z_α is given by the measurements described in Ref. 12. The electron density across the plasma shell was determined from the Stark broadening of spectral line pro-

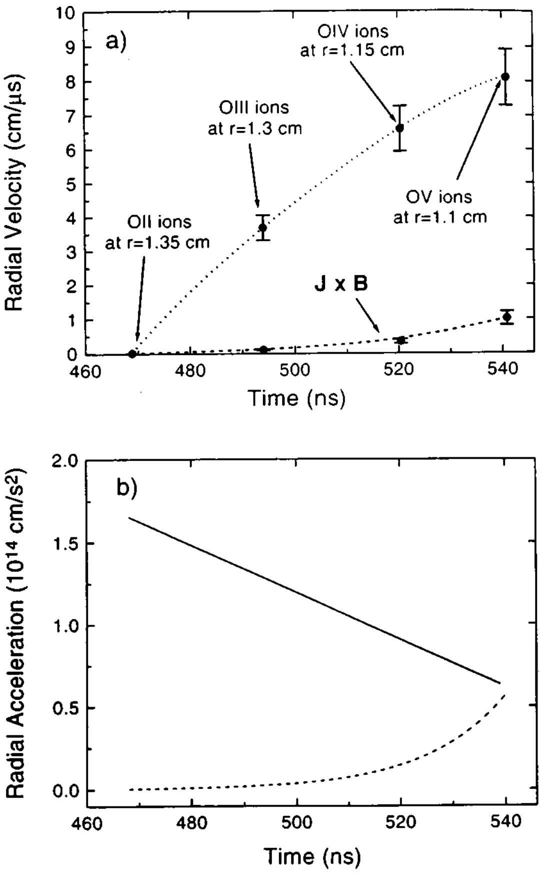

FIG. 10. (a) Measured velocity of a fluid element that is encountered by the ionization front at $t=470$ ns and $r=1.35$ cm, obtained from the previously measured (Ref. 12) radial velocities of the various charge state ions across the plasma shell. The dotted line is a smooth monotonic curve through the data points. The dashed line is the calculated accumulated contribution of the $\mathbf{J}\times\mathbf{B}$ forces in the plasma to the time-dependent velocity of the same fluid element. For completeness we indicate by the arrows the times and the corresponding radial locations at which this fluid element is dominated by the respective ionization stages. (b) The total radial acceleration as a function of time of the fluid element (solid line), together with the calculated radial acceleration only due to the $\mathbf{J}\times\mathbf{B}$ forces (dashed line). Both curves are obtained by derivation of the velocity curves given in (a).

files, as described in Ref. 15. This allows $F_R(r,t)$ to be calculated, thus giving the ion radial velocity V_α that would have resulted only from the $\mathbf{J}\times\mathbf{B}$ forces, at times $t>t_0$

$$V_\alpha(r(t),t)=\int_{t_0}^{t}\frac{d\tau}{m_i}\,F_R(r(\tau),\tau), \tag{8}$$

where m_i is the ion mass and $r(\tau)$ is the radial position of the fluid element at time τ. Example of the histories of V_α and v_α for a fluid element that is encountered by the ionization front at $t=470$ ns and $r=1.35$ cm are shown in Fig. 10(a). Given in Fig. 10(b) are the time-dependent total acceleration of the fluid element $\mathbf{a}_{\rm tot}$, and the acceleration due to the magnetic pressure $\mathbf{a}_{\mathbf{J}\times\mathbf{B}}$, both obtained from the velocity curves in Fig. 10(a). It is seen that until $t\simeq 520$ ns, when the ions are still relatively far from the outer boundary of the plasma, the radial acceleration due to the $\mathbf{J}\times\mathbf{B}$ force is negligible, i.e., the ion acceleration is caused by the thermal pressure. The average value of the thermal pressure gradient for $480<t<540$ ns is $\nabla P=m_i n_i[\mathbf{a}_{\rm tot}-\mathbf{a}_{\mathbf{J}\times\mathbf{B}}]\sim 5\times 10^8$ dyn/cm^3. The magnetic pressure becomes dominant $[\mathbf{a}_{\mathbf{J}\times\mathbf{B}}\sim\mathbf{a}_{\rm tot}$, see Fig. 10(b)] at later times, when the particles are highly ionized and are located closer to the outer boundary of the plasma. For example, at $t\simeq 535$ ns, the **OV** ions, mainly accelerated by the magnetic pressure, are located at $r=1.1$ cm, where the outer boundary R_0 is at 1.15 cm.

Following this procedure for different fluid cells it is possible to obtain a complete mapping (r,t) of the thermal pressure across the plasma shell. This, together with a hydrodynamic modeling and a detailed study of the energy balance in the z-pinch plasma, will be presented in a separate publication.

VI. SUMMARY

We have determined the radial distribution of the magnetic field as a function of time during the implosion phase of a CO_2 gas-puff z-pinch plasma by observing the contribution of the Zeeman effect to the line-emission spectral profiles of various charge-state oxygen ions across the plasma shell. Since the line profiles are dominated by Stark broadening, polarization spectroscopy and high-accuracy line-profile measurements were required. It was found that most of the circuit current flows through the imploding plasma, and that the field penetration into the plasma can be satisfactorily explained based on classical diffusion. It is also shown that the experimental determination of the time-dependent magnetic-field distribution in the plasma, together with the ion radial velocities measured from line Doppler shifts, allow for obtaining the thermal pressure gradient in the plasma. Furthermore, the current density distribution and the electrical conductivity obtained from the time-dependent magnetic-field distribution allow for the determination of the Joule heating rate across the plasma shell. The experimentally determined time-dependent radial distributions of the various heating terms are currently being compared to the results of collisional-radiative and magnetohydrodynamic calculations, and will be presented in detail in a future study.

We believe that spatially resolved measurements, based on the observation of Zeeman splitting at various spectral ranges, can be useful for studying the interaction between dense plasmas and strong magnetic fields in various pulsed-power experiments.

ACKNOWLEDGMENTS

It is a pleasure to thank A. Fisher for very helpful discussions on the experiment, and to H. R. Griem for his critical comments and for reading the manuscript. We are also grateful to Y. Ralchenko for his help in the collisional-radiative calculations, and to V. Fisher, A. Fruchtman, B. Peter, C. Litwin, J. Davis, W. Thornhill, R. N. Sudan, M. G. Haines, and H.-J. Kunze for valuable comments. The skilled technical assistance of P. Meiri is highly appreciated.

This work was supported by the Minerva Foundation (Munich, Germany), the Israeli Academy of Science, and by the Binational Science Foundation (U.S.).

[1] N. R. Pereira and J. Davis, J. Appl. Phys. **64**, R1 (1988).
[2] T. W. L. Sanford, G. O. Allshouse, B. M. Marder, T. J. Nash, R. C. Mock,

R. B. Spielman, J. F. Seamen, J. S. McGurn, D. Jobe, T. L. Gilliland, M. Vargas, K. W. Struve, W. A. Stygar, M. R. Douglas, M. K. Matzen, J. H. Hammer, J. S. De Groot, J. L. Eddleman, D. L. Peterson, D. Mosher, K. J. Whitney, J. W. Thornhill, P. E. Pulsifer, J. P. Apruzese, and Y. Maron, Phys. Rev. Lett. **77**, 5063 (1996).

[3] M. G. Haines, Phys. Scr. **T2/2**, 380 (1982).

[4] C. W. Hartman, J. L. Eddleman, R. Moir, and U. Shumlak, Fusion Technol. **26**, 1203 (1994).

[5] H. R. Bolton, P. Choi, A. E. Dangor, A. J. H. Goddard, M. G. Haines, S. G. Peerless, A. Power, and S. P. Walker, Fusion Eng. Des. **10**, 9 (1989).

[6] J. J. Rocca, V. Shlyaptsev, F. G. Tomasel, O. D. Cortázar, D. Hartshorn, and L. A. Chilla, Phys. Rev. Lett. **73**, 2192 (1994).

[7] J. Bailey, Y. Ettinger, A. Fisher, and R. Feder, Appl. Phys. Lett. **40**, 33 (1982).

[8] M. Tanaka, H. Kawata, and K. Murata, Jpn. J. Appl. Phys. **28**, 1250 (1989).

[9] V. V. Vikhrev and S. I. Braginskii, in *Reviews of Plasma Physics*, edited by M. A. Leontovich (Consultants Bureau, N.Y., 1986), Vol. X, p. 425.

[10] K. N. Koshelev and N. R. Pereira, J. Appl. Phys. **69**, R21 (1991).

[11] G. S. Sarkisov, A. S. Shikanov, B. Etlicher, S. Attelan, C. Rouille, and V. V. Yan'kov, JETP **81**, 743 (1995).

[12] M. E. Foord, Y. Maron, G. Davara, L. Gregorian, and A. Fisher, Phys. Rev. Lett. **72**, 3827 (1994).

[13] S. Alexiou, Phys. Rev. A **49**, 106 (1994); S. Alexiou, J. Quant. Spectrosc. Radiat. Transf. **51**, 849 (1994); S. Alexiou, and Yu. Ralchenko, Phys. Rev. A **49**, 3086 (1994).

[14] L. Gregorian, M.Sc. Thesis, Feinberg Graduate School, Weizmann Institute of Science (1993).

[15] G. Davara, Ph.D. Thesis, Feinberg Graduate School, Weizmann Institute of Science (1995).

[16] A. N. Tikhonov and A. A. Samarski, *Partial Differential Equations of Mathematical Physics* (Holden-Day, San Francisco, California, 1964).

[17] N. A. Krall and A. W. Trivelpiece, *Principles of Plasma Physics* (McGraw-Hill, New York, 1973).

[18] R. C. Davidson and N. T. Gladd, Phys. Fluids **18**, 1327 (1975); R. C. Davidson and N. A. Krall, Nucl. Fusion **17**, 1313 (1977).